STRUCTURAL DESIGN AND VISION-BASED TARGET DETECTION AND LOCALIZATION OF A DESERT SHRUB STUBBLE-CUTTING MACHINE
/
沙生灌木平茬机的结构设计与基于视觉的目标检测与定位

Weiqi WU[1], Haitang CEN*[1], Wang GUO[2], Wei ZHANG[1]
[1] School of Mechanical Engineering, Inner Mongolia University of Technology, Hohhot, 010000 / China;
[2] Inner Mongolia Academy of Science and Technology, Hohhot, 010000 / China
Tel: +86-13514712360; E-mail: 1054949591@qq.com
DOI: https://doi.org/10.35633/inmateh-79-26

Keywords: *desert shrubs, machine vision, structural design, stubble cutting machine*

ABSTRACT
Current research on shrub stubble cutting machines primarily focuses on mechanical structure design and operational performance, whereas shrub localization and cutting status still rely on manual judgment. To address this issue, an intelligent desert shrub stubble cutting machine integrating structural design with vision-assisted operation was developed. The overall structure and key component parameters were determined through theoretical analysis, and the disc cutting process was validated via Workbench simulation. The YOLOv5s model incorporating a Focal-CIoU loss function was adopted to enhance shrub detection under complex background conditions. Image processing and binocular vision were employed to obtain the three-dimensional coordinates of shrub roots. Experimental results demonstrate that the cutting device meets the operational requirements; the improved model achieves an accuracy of 91.9%, a recall of 96.5%, and a mAP of 98.3%; and the maximum relative errors for root depth and height measurements are 3.19% and 6.51%, respectively, satisfying the detection and localization requirements for shrub stubble cutting.

摘要
当前灌木平茬机的研究主要集中于机械结构设计与作业性能，而灌木定位和切割状态仍依赖人工判断。针对该问题，本文研制了一种将结构设计与视觉辅助作业相结合的智能荒漠灌木割茬机。通过理论分析确定了整机结构和关键部件参数，并利用Workbench 仿真验证了圆盘切割过程。采用引入Focal-CIoU 损失函数的YOLOv5s 模型，以增强复杂背景条件下的灌木检测能力。利用图像处理和双目视觉获取了灌木根部的三维坐标。实验结果表明：切割装置满足作业要求；改进模型的准确率达到 91.9%，召回率为 96.5%，mAP 为 98.3%；根部深度和高度测量的最大相对误差分别为 3.19%和 6.51%，满足灌木平茬检测与定位要求。

INTRODUCTION
Land desertification represents a major obstacle to ecological restoration and sustainable development. As of 2024, desertified land in China accounts for approximately 26.8% of the country's total terrestrial area. Xerophytic shrubs, such as *Salix psammophila* and *Haloxylon ammodendron*, are widely used for windbreak and sand fixation as well as ecological restoration due to their pronounced drought tolerance and significant sand-binding capacity (*Gao S. et al., 2022*). These shrubs exhibit a growth characteristic known as "rejuvenation after pruning": prolonged absence of pruning leads to gradual branch senescence and even whole-plant mortality, which may in turn induce secondary desertification (*Pei et al., 2019*). Therefore, regular pruning is an essential measure to maintain the long-term vitality of these shrubs. At present, pruning of xerophytic shrubs in China relies predominantly on manual labor and semi-automatic backpack pruning machines, which suffer from low operational efficiency and high labor intensity. Moreover, prolonged use is associated with occupational health risks, including vibration-induced disorders and noise-induced hearing loss (*Tian, 2013*).

Existing research on pruning machines has primarily focused on mechanical structures and operational parameters. *Ma et al., (2015),* developed a tracked, self-propelled shrub pruning machine that improved adaptability to sandy terrain through a floating cutting mechanism. *Wang et al., (2025),* designed a hydraulic scissor-type Caragana pruning machine and reduced both branch breakage rate and cutting power consumption via parameter optimization. Although these studies have enhanced the operational performance of the equipment, the pruning process remains largely manual, with limited perception of shrub distribution and ground surface variations.

Regarding intelligent pruning operations, *Ren (2021)* integrated machine vision into Caragana pruning tasks, enabling the identification of root collar positions and supporting adaptive adjustment of the cutting platform height. However, this work focused on visual recognition in isolation and lacked full integration with the machine's structural design and practical operational workflows. In agricultural machinery research, machine vision has been successfully applied to identification and localization tasks in field operations—for example, *Fan et al., (2025),* achieved cotton row detection for spraying robots in cotton fields. Nevertheless, these studies targeted regularly spaced row crops, whose spatial distribution differs markedly from the sparse, irregular, and clustered arrangement of desert shrubs, rendering the direct transfer of such methods impractical for shrub pruning applications.

To address the aforementioned challenges, this paper proposes the design of an intelligent pruning machine for xerophytic shrubs. The machine is built upon a tracked mobile platform and integrates cutting and baling functions. It incorporates a visual recognition system based on an improved YOLOv5s model, synergistically combining image processing with binocular stereo vision measurement. Simulation analyses and prototype experiments were conducted to validate the machine's capabilities in accurate shrub identification, three-dimensional localization, and adaptive cutting. The findings provide a technical reference for the development of intelligent pruning equipment for xerophytic shrubs.

MATERIALS AND METHODS

Machine structure design

The intelligent shrub-topping machine developed in this study consists of a cutting unit, a baling unit, a binocular stereo camera, a tracked locomotion system, a conveying mechanism, a header lifting mechanism, a motor, and a battery. The overall configuration and key design parameters are illustrated in Fig. 1 and listed in Table 1, respectively (*Zhang B. et al., 2022; Georges R. et al., 2014*).

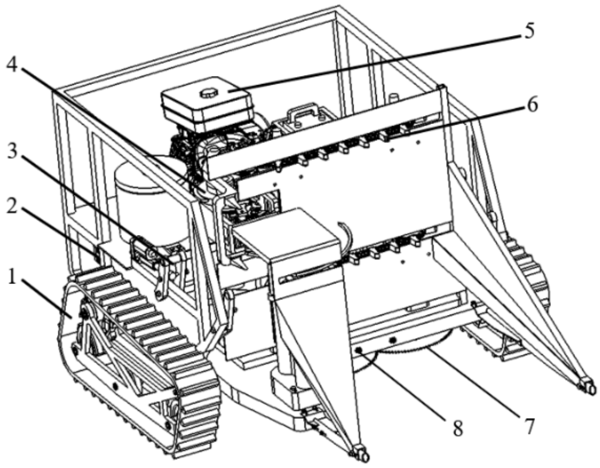

Fig. 1 - Overall structure of the shrub stubble cutting machine

1 – Traveling mechanism; 2 – Traveling drive assembly; 3 – Header lifting device; 4 – Baling device; 5 – Powertrain; 6 – Conveying device; 7 – Cutting device; 8 – Binocular camera sensor

Table 1

Technical parameters of the shrub trimmer for sandy land

Parameter	Value
Overall machine weight (kg)	<500
Overall dimensions (length × width × height) (mm)	1450×1342×1000
Diameter of coppiced shrubs (mm)	0~20
Working width (mm)	700
Pruning height (mm)	10-100
Power of a single travelling motor (kW)	2

Operating principles

During operation, the rubber-tracked chassis propels the machine toward the target shrub stand. The cutting platform height is adjusted to a preset cutting position via an electric linear actuator (*Johnson P.C. et al., 2012*), after which the cutting motor is activated.

As the machine advances, the V-shaped guide plate mounted at the front end aligns and directs the shrubs, facilitating smooth entry into the cutting zone and enabling precise severance. The cut shrubs are continuously conveyed into the baling unit by a conveyor chain and progressively compacted under the compressive force exerted by the baling tines. Once the diameter of the shrub bundle within the baling unit reaches a preset threshold, the baling clutch engages automatically; the rope feed needle then delivers twine to the knotting mechanism to complete the binding process. Subsequently, the bound shrub bundle is ejected laterally from the machine. The clutch then disengages, and the baling unit ceases operation, thereby completing one full pruning cycle.

Main structure design of the cutting device

The cutting unit is one of the most critical components of the brush cutter designed for xerophytic shrubs. In this study, a disc-type cutting unit is adopted, as illustrated in Fig. 2. The cutting platform is connected to the frame via a four-bar linkage and secured with bolts. Power from the cutting motor is transmitted to the main shaft, and the ground clearance of the cutting unit is regulated by the extension and retraction of electric linear actuators mounted on both sides of the frame.

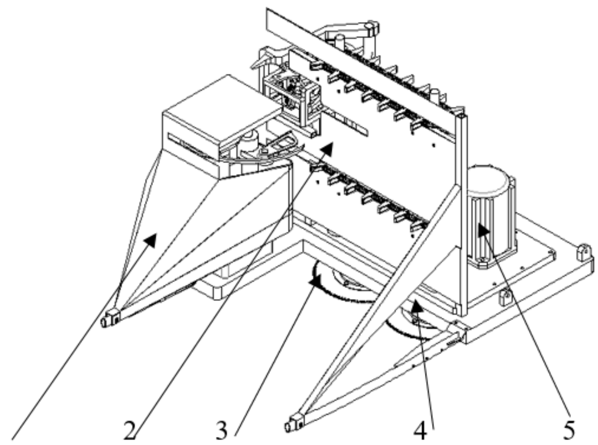

Fig. 2 - Schematic diagram of the cutting unit
1 – Branch gathering frame; 2 – Cutting baffle; 3 – Cutting component; 4 – Bottom plate drive; 5 – Cutting motor

Design and calculations of the cutting unit

1) Transmission system design

The transmission system of the cutting unit consists of gears, sprockets, and transmission shafts. Power from the motor is transmitted to cutting spindles I and II via gear trains. Spindle I additionally transmits power to the conveying unit and the baling unit to facilitate transport and compaction of the severed shrubs. The corresponding schematic diagram is presented in Fig. 3. At the lower end of the extended shaft of spindle I, the cutter head is attached, while the upper end is coupled to the gearbox via a keyway, enabling power transmission to the conveying unit.

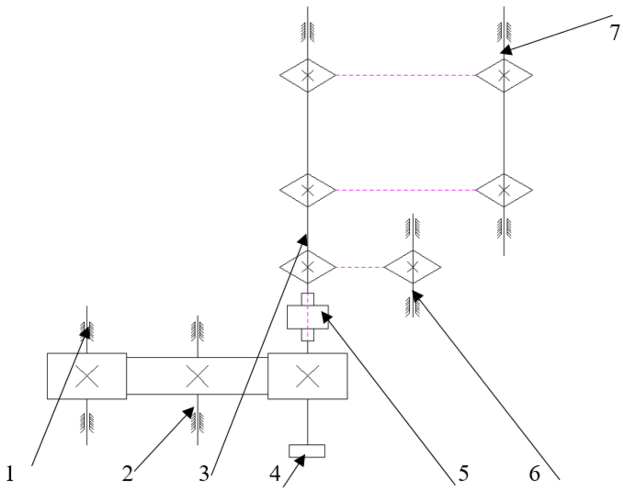

Fig. 3 - Schematic diagram of the transmission system
1 – Power input shaft; 2 – Intermediate shaft; 3 – Drive shaft of transmission chain; 4 – Cutting component; 5 – Planetary reducer; 6 – Power input shaft of baling mechanism; 7 – Transmission shaft of transmission chain

2) Circular saw blade selection

The principal parameters of the saw blade include the outer diameter D, thickness S, number of teeth T, rake angle γ_1, and clearance angle α_1. Based on the diameter of the shrub roots and in accordance with circular saw blade standards, the blade diameter is selected as D = 350 mm. The thickness of the blade is determined by Equation (1):

$$S = \eta_1 K \sqrt{D} \tag{1}$$

where:

η_1 is the safety factor, taken as 1.68; K is the thickness safety coefficient, taken as 0.075. After calculation, the thickness S of the circular saw blade is determined to be 2.3 mm. The number of teeth T is 100, the rake angle γ_1 is 20°, and the clearance angle α_1 is 15°.

3) Calculation of cutting power

The total power P_Z consumed during shrub cutting consists of the no-load rotational power P_K of the saw blade and the cutting power P_L. The corresponding formulas for calculating these three power components are given in Equations (2) - (4):

$$P_k = \frac{mv_c^2 + J\omega^2}{2} \tag{2}$$

$$P_L = \frac{v_f Al}{102} \tag{3}$$

$$P_Z = P_K + P_L \tag{4}$$

where:

m is the mass of the circular saw blade, 1.625 kg; v_c is the peripheral speed of the saw blade, 26 m/s; J is the moment of inertia of the saw blade, 0.49 kg·m^2; ω is the angular speed of the saw blade, rad/s; v_f is the feed velocity of the brush cutter, 0.5 m/s; A is the cutting width, m; l is the specific cutting energy required for shrubs, 490 J/m^2. Finally, P_K is 0.82 kW, P_L is 0.84 kW, and P_Z is 1.66 kW.

Main structure and working principle of the baling unit

This study adopts a side-baling configuration. The baling unit consists of a knotter, a power input chain, the knotter main shaft, a rope feed rocker, a rope feed rocker transmission shaft, and a stem compression rod. The power input shaft of the baling unit is connected to the conveyor chain main shaft via a chain drive. When the clutch lever is actuated—i.e., depressed and rotated by a specified angle—the power input shaft engages with the knotter main shaft, thereby initiating knotter operation. The rope feed rocker main shaft and the knotter main shaft are interconnected by a chain drive. The transmission chain is housed within the baseplate, and the chain type selected is the C08A roller chain. A schematic diagram of the baling unit is presented in Fig. 4.

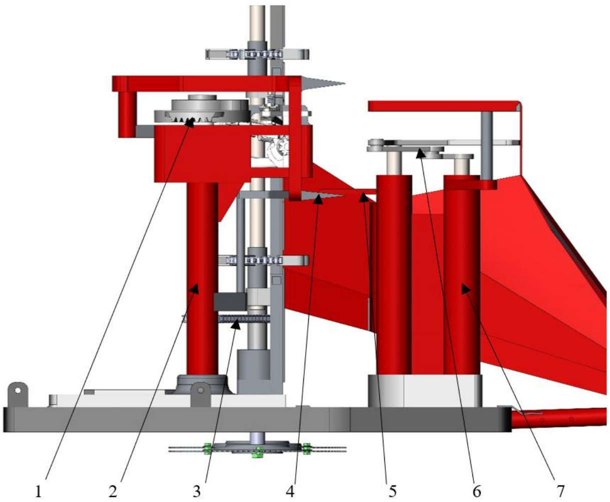

Fig. 4 - Structure of the baling mechanism

1 – Knotting device; 2 – Drive shaft sleeve I; 3 – Power input chain; 4 – Clutch control lever; 5 – Stem-pressing rod; 6 – Rope-feeding rocker; 7 – Drive shaft sleeve II

Design of the main components of the baling unit

1) Design of the knotter structure

The knotter consists of a conical gear disc, a rope-clamping device, and knotting pliers, as illustrated in Fig. 5. The phase difference between the inner and outer teeth of the conical gear disc is 58°, which governs the timing coordination between the rope-clamping device and the knotting pliers. The phase difference between the outer teeth and the cam's far stop point is 111°, which controls the timing coordination between the knotting pliers and the rope-cutting knife.

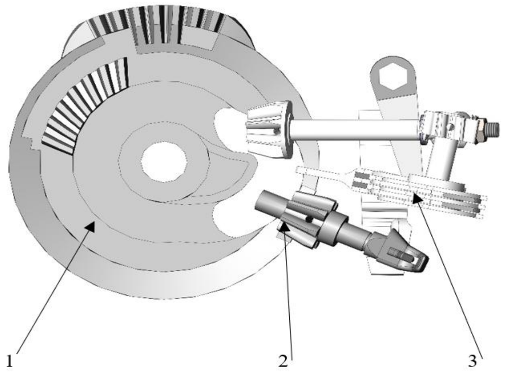

Fig. 5 - Structure of the knotting mechanism
1 – Conical-toothed disc; 2 – Looping pliers; 3 – Rope clamp

2) Design of the rope-feeding rocker

The rope feed rocker, as the most critical auxiliary component of the baling unit, is designed to deliver rope accurately and rapidly to the knotter, thereby facilitating the baling operation. To minimize the time required for rope feeding and baling, a crank-rocker mechanism is adopted in the design of the rope feed rocker. A simplified motion analysis diagram is presented in Fig. 6 (*Mutlu H., 2021*). Based on this diagram, the motion parameters of the rocker can be determined. Through empirical design, the rotation radius of the driving crank l_1 is set to 63 mm. Using the crank-rocker mechanism calculation formulas, the lengths of the remaining three links—l_2, l_3, and l_4—are determined as 124 mm, 124 mm, and 134 mm, respectively.

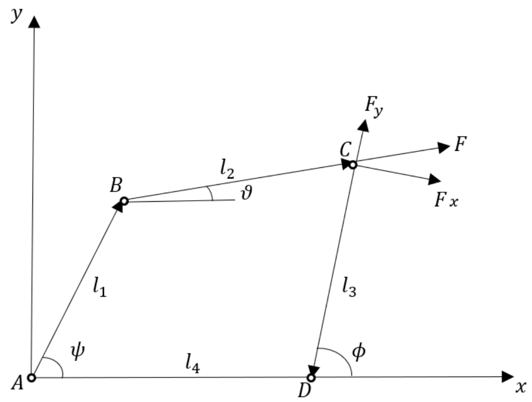

Fig. 6 - Force diagram of the crank-rocker mechanism

Simulation analysis on the stubble-cutting process of the cutting device

To ensure the accuracy of the simulation results while maintaining computational efficiency, the following simplifications were applied to the circular-disc cutting model: (1)The cross-section of the desert shrub was approximated as a circular profile; (2) The taper variation along the shrub stem was neglected, and the stem was modelled as a cylinder of uniform cross-sectional area; (3)The upper and lower clamping plates, transmission system, and bolts of the circular saw blade were omitted, and the bolt mounting holes were removed (*Wu G., Zhang D.D., 2022*).

Based on the aforementioned simplifications, the model was developed using SolidWorks. The saw blade was modelled with a diameter of 350 mm, a rake angle γ_1 = 20°, the clearance angle α_1 = 15°, and a tooth count T=100. As the primary target of cutting in this study was shrubs with a stem height of 0–20 mm, the shrub was simplified as a cylinder of 20 mm diameter and 200 mm height, with the cutting height set to 70 mm.

In Workbench, the material of the circular saw blade was defined as 65Mn steel, with a density of 7.85×10^3 kg/m³, a Poisson's ratio of 0.3, and an elastic modulus of 210 GPa. Desert shrub stems are characterized as nonlinear, non-homogeneous, and anisotropic elastic materials (*Gangwar T., Schillinger D., 2019*). To reduce model complexity while satisfying the analysis requirements, the stem was simplified as an isotropic linear-elastic material. The corresponding material parameters were assigned from the Workbench material library as follows: density of 480 kg/m³, Poisson's ratio of 0.33, and elastic modulus of 5034 MPa. The stress distribution cloud diagram obtained from the simulation is presented in Fig. 7.

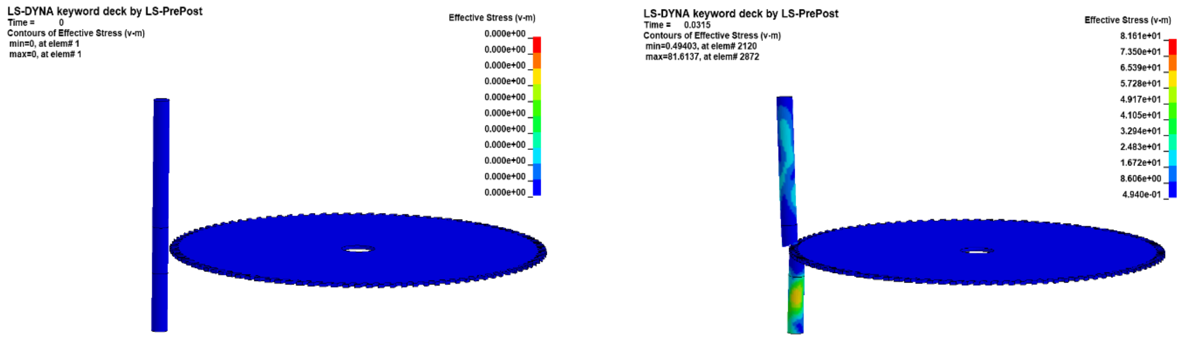

a. Initial moment of the simulation b. Moment of shrub cutting

Fig. 7 - Stress variation during the four stages of the simulated sawing process

The curves of total cutting force, required energy, and cutting power of the circular saw blade over time during shrub cutting are presented in Fig. 8. As shown in Fig. 8a, the maximum total cutting force acting on the shrub stem reaches 13 N at a simulation time of 0.175 s. From Fig. 8b, it can be observed that cutting initiates at 0.026 s; the shrub stem bends under load and accumulates strain energy. At 0.03 s, the stem releases all the stored energy due to elastic deformation. The maximum energy required for cutting the shrub is 13 J. As illustrated in Fig. 8c, the maximum power required for cutting is 1670 W, which is consistent with the power consumption obtained from the theoretical calculation presented earlier. These simulation results indicate that the cut-ting device designed in this study meets the operational requirements for shrub cutting.

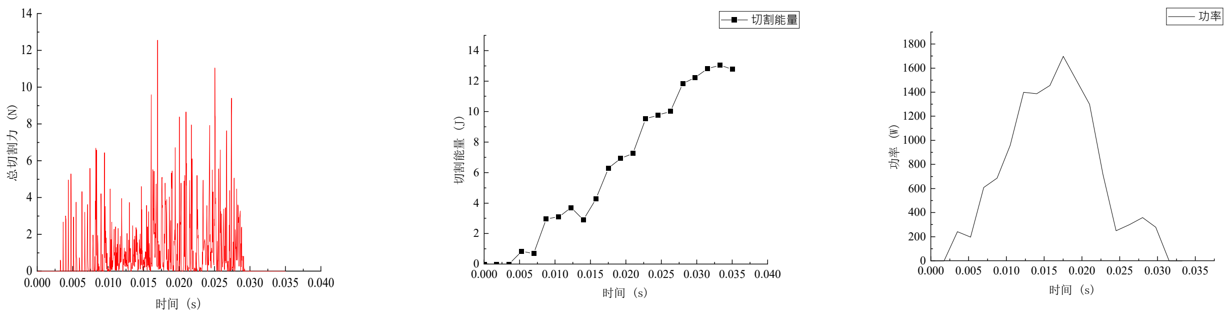

a. Total cutting force b. Cutting energy c. Cutting power

Fig. 8 - Curve of energy change during shrub cutting

Model training and evaluation of the visual recognition algorithm

Following the structural design of the pruning machine and the simulation analysis of the cutting components, this study investigates an image recognition algorithm for shrub detection during pruning operations. Model training and testing were conducted in a Windows 11 environment using a 12th Gen Intel(R) Core(TM) i5-12490F processor, an NVIDIA GeForce RTX 3060 Ti graphics card, 16 GB of RAM, and Python version 3.10.

In this experiment, 50 images were collected through online image retrieval and manual capture. The dataset was then augmented using techniques including horizontal flipping, brightness adjustment, rotation, scaling, cropping, high-frequency noise addition, Gaussian blurring, and histogram equalization. The final augmented shrub image dataset comprised 1,000 images and was randomly partitioned into training, validation, and test sets in an 8:1:1 ratio, corresponding to 80% for training, 10% for validation, and 10% for testing. During model training, the batch size was set to 8, the initial learning rate to 0.01, the weight decay coefficient to 0.0005, the momentum factor to 0.937, and the total number of epochs to 150.

Focal-CIoU-based improved loss function

In the original YOLOv5s network architecture, Complete Intersection over Union (CIoU) is employed as the bounding box regression loss function. CIoU quantifies the degree of matching between predicted and ground-truth bounding boxes by jointly considering the intersection over union (IoU), the Euclidean distance between their center points, and the consistency of their aspect ratios (*Li T. et al., 2023*). The corresponding formulas are given in Equations (5) - (7):

$$\begin{aligned} L_{CIoU} &= 1 - \mathrm{IoU} + \frac{\rho^2\left(b, b^{gt}\right)}{c^2} + \alpha v \\ &= 1 - \frac{\left|B \cap B^{gt}\right|}{\left|B \cup B^{gt}\right|} + + \frac{\rho^2\left(b, b_{gt}\right)}{c^2} + \alpha v \end{aligned} \tag{5}$$

$$v = \frac{4}{\pi}(\arctan\frac{w}{h} - \arctan\frac{w}{h}) \tag{6}$$

$$\alpha = \frac{v}{(1 - \mathrm{IoU}) + v} \tag{7}$$

where:

IoU is the intersection over union between the predicted box and the ground-truth box; B and B^{gt} are the predicted box and the ground-truth box, respectively; b and b^{gt} are the centers of B and B^{gt}, respectively; ρ^2 is the squared Euclidean distance between the two centers; c is the diagonal length of the smallest enclosing rectangle covering both boxes; α is the control parameter for the convergence speed of the loss; v is the measure of the aspect ratio difference.

In practical shrub detection, the sparse distribution of shrubs in desert environments results in some collected images where the shrubs occupy a significantly smaller proportion of the image area compared to the desert background. This imbalance hinders the model's ability to effectively learn discriminative shrub features, thereby reducing detection accuracy. To address this issue, this study adopts the computational principle of Focal Loss and integrates it with CIoU to formulate the Focal-CIoU loss function (*Peng H. et al., 2023*), as presented in Equation (8):

$$L_{Focal-CIoU} = IoU^{\gamma} L_{CIoU} \tag{8}$$

where:

γ represents the degree of outlier suppression.

By introducing the IoU modulation term, Focal-CIoU reduces the influence of samples with high IoU values in the loss computation, enabling the model to focus more on shrub targets with large localization errors during training—thereby improving localization accuracy and detection performance in complex backgrounds.

Experimental results and analysis of the visual recognition algorithm

To evaluate the shrub detection performance of the improved YOLOv5s network, comparative experiments were conducted using YOLOv5s, YOLOv7-Tiny, YOLOv8s, as well as the lightweight backbones MobileNetV3 and ShuffleNetV2 integrated into the YOLOv5 framework. All models were trained under identical conditions using the same dataset. The experimental results are presented in Table 2.

Table 2

Comparison of detection performance across different models

Models	Precision [%]	Recall [%]	mAP@0.5 [%]	Params [M]	FLOPs [G]
YOLOv5s	91.1	94.3	97.7	7.01	15.8
YOLOv7-Tiny	91.4	91.2	96.4	6.14	13.6
YOLOv8s	91.8	92.4	96.8	11.12	28.4
MobileNetV3	73.8	85.3	85.4	2.39	3.5
ShuffleNetV2	75.2	77.0	82.3	1.8	2.8
This paper	91.9	96.5	98.3	7.01	15.8

As shown in Table 2, YOLOv8s achieves the highest accuracy among all models evaluated; however, it also has the largest number of parameters and the highest computational cost, making it the most complex model.

Although MobileNetV3 and ShuffleNetV2 have fewer parameters and lower computational costs, their accuracy is insufficient to ensure reliable detection performance. The improved model achieves higher accuracy and recall than all other detection models in the experiment. Compared with YOLOv5, YOLOv7‑Tiny, and YOLOv8s, the improved model increases accuracy by 0.8, 0.5, and 0.1 percentage points, respectively, and recall by 2.2, 5.3, and 4.1 percentage points, respectively. Therefore, the proposed network model not only achieves higher accuracy and recall but also has fewer parameters and lower computational cost, making it more suitable for deployment on brush cutters for shrub detection.

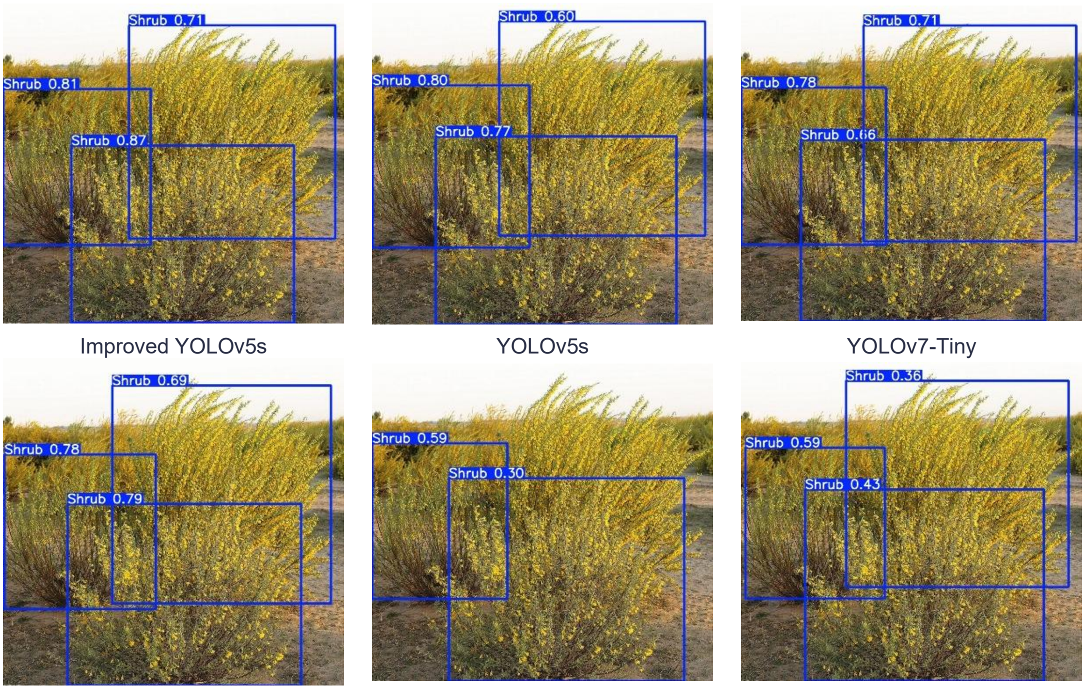

Improved YOLOv5s YOLOv5s YOLOv7-Tiny

YOLOv8s MobileNetv3 ShuffleNetV2

Fig. 9 - Shrub detection results across different network models

Figure 9 presents the shrub detection results of the six models. With the exception of ShuffleNetV2, which missed one shrub, all other models correctly detected three shrubs. Among them, the detection confidence of MobileNetV3 was significantly lower than that of the remaining four models, indicating weaker detection performance. Compared with the other network models, the improved YOLOv5s model achieves more accurate shrub localization and higher confidence scores, demonstrating superior detection performance.

Image processing-based shrub root detection and 3D measurement method

The shrub root image processing algorithm employs digital image processing techniques to isolate shrub root branches from complex backgrounds. To remove irrelevant information, the acquired image undergoes a series of preprocessing steps. First, the image is converted to grayscale using the maximum intensity method (*Chun P.J. et al., 2021*) to enhance the contrast between roots and background. Second, median filtering is applied for noise suppression (*Cao et al., 2024*). Third, Otsu's thresholding method (*Hu J. et al., 2024*) is used for segmentation, followed by intensity inversion to highlight root contours. Finally, a morphological closing operation (consisting of erosion followed by dilation) with a 10×10 structuring element (*Zhou R.G. et al., 2015*) is performed to suppress shadows and residual leaf fragments. The largest connected foreground region is then selected, and its contour is outlined in green to complete shrub root segmentation. The complete processing pipeline is illustrated in Fig. 10.

a. Original shrub image b. Grayscale conversion using maximum intensity projection c. Median-filtered image

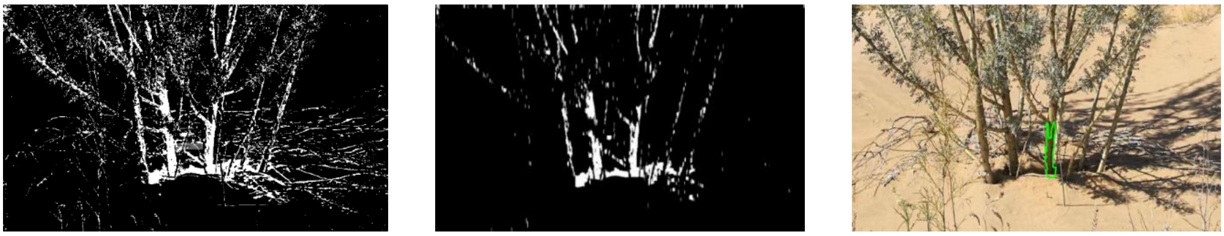

d. Otsu-thresholded binary image e. Morphologically closed image f. Root segmentation result

Fig. 10 - Image processing process of shrub roots

Experimental validation of shrub root localization accuracy

Using the parallax between the left and right cameras of the binocular stereo system and applying the principle of similar triangles, the distance from each three-dimensional scene point to the camera is computed (*Ren Z. et al., 2022; Hu W. et al., 2021; Zhai G. et al., 2020*). Camera calibration is then performed to estimate the intrinsic and extrinsic camera parameters and to correct lens distortion (*Wang Q. et al., 2022*). Finally, the Semi-Global Block Matching (SGBM) algorithm is employed for stereo correspondence, yielding the depth maps shown in Figs. 11a and 11b (*Almatrouk B. et al., 2024*).

The three-dimensional coordinate visualization of the shrub in the image is presented in Fig. 11c, where the y-axis represents the vertical height of the shrub relative to the camera plane, and the z-axis represents the depth (i.e., the distance along the optical axis) from the camera.

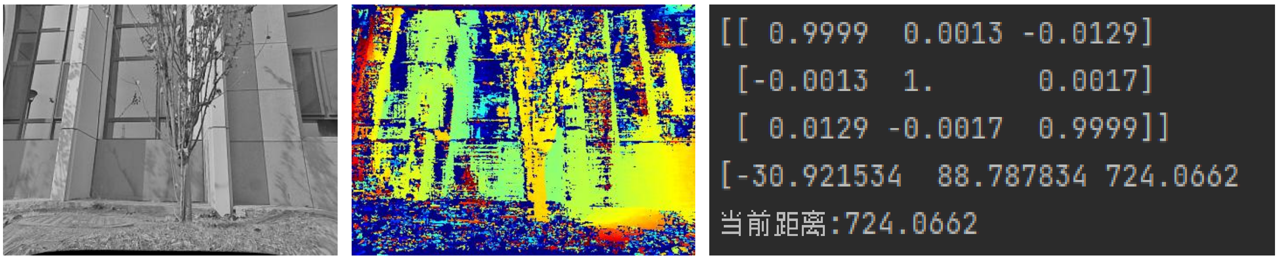

a. Grayscale shrub image b. Shrub depth map c. Coordinate Output Diagram

Fig. 11 - Grayscale and depth images of shrubs in the test scene

RESULTS

Construction and experimental validation of a simplified shrub stubble-cutting prototype

The simplified prototype of the pruning machine developed in this study is shown in Fig. 12a. Its main components include a gear reducer and a DC motor, a Raspberry Pi microcontroller unit, an STM32-based expansion board, a binocular stereo camera, an ultrasonic distance sensor, and a power supply unit.

Shrub detection experiment

In this experiment, an area with shrub vegetation on a university campus was selected as the test site, and the pruning machine prototype was deployed at the location shown in Fig. 12b. The prototype is equipped with YOLOv5s for real-time object detection, enabling the acquisition of image and spatial coordinate information. The shrub recognition results are presented in Fig. 12c, which demonstrates that the prototype achieves robust shrub detection performance.

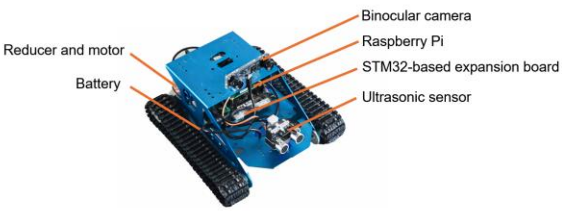

a. Simple Model of the Flushing Machine

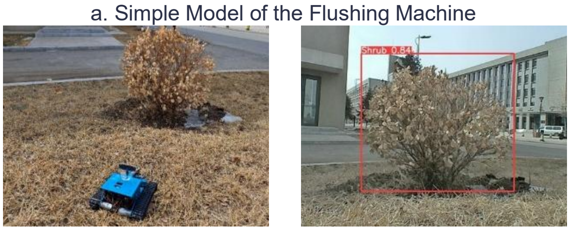

b. Experimental environment c. Recognition result

Fig. 12 - Shrub identification experiment

Image processing-based shrub root detection experiment

To verify the effectiveness of the image processing algorithm, further processing was performed on the image containing the shrub with the largest bounding box area, thereby providing data support for shrub pruning. The shrub root detection results are presented in Fig. 13. As shown in the resulting images, the image preprocessing and morphological operations are effective, and the detection outcomes are accurate.

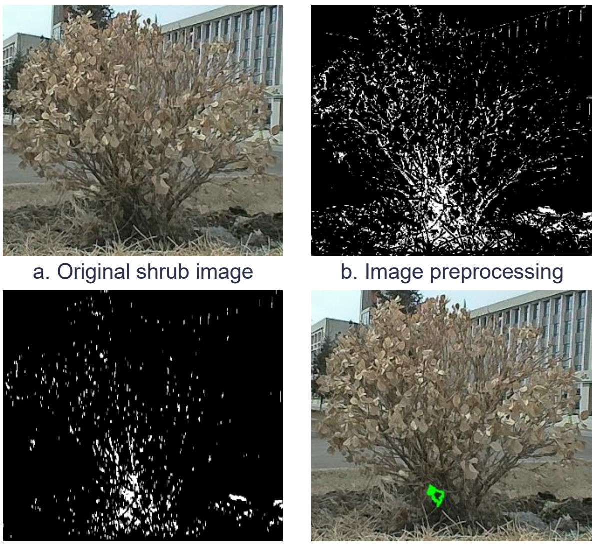

a. Original shrub image b. Image preprocessing

c. Morphological operations d. Detection results

Fig. 13 - Results of the shrub root detection experiment

Experimental validation of shrub root localization accuracy

To verify the effectiveness of the proposed shrub root detection algorithm, images were captured using a binocular camera, and feature points were matched via the Semi‑Global Block Matching (SGBM) algorithm. A depth map was then reconstructed based on binocular stereo vision principles. The experimental results are presented in Figs. 14a and 14b.

The depth image and the shrub root identification image were overlaid to integrate the root detection results into the shrub's depth map and to output the coordinates of the center point. The measured shrub root height and depth are shown in Fig. 14c, where the center point height corresponds to the vertical coordinate of the center of the shrub root bounding box relative to the camera plane. The relative errors in this trial were 2.51% for depth measurement and 5.59% for height measurement.

To evaluate the reliability of the algorithm for shrub depth and height estimation, 12 independent trials were conducted following the same procedure. The three‑dimensional coordinates of each detected root center were extracted and compared against ground‑truth distance and height measurements. The detailed results are listed in Table 3. The experimental results indicate that the maximum relative errors in depth and height estimation are 3.19% and 6.51%, respectively—both within the tooling alignment tolerance required for precise shrub cutting by the hedger.

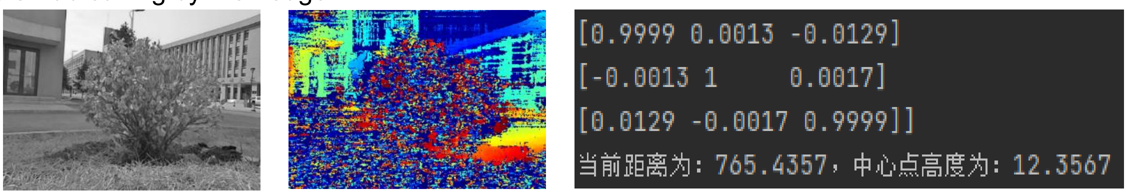

a. Grayscale shrub image b. Shrub depth map c. Three-dimensional shrub root coordinate visualization

Fig. 14 - Experimental results of shrub depth map drawing

CONCLUSIONS

Based on the operational requirements for pruning sand‑dwelling shrubs, this study completed the overall structural design of the pruning machine and the selection of key component parameters. A simulation analysis of the circular‑saw cutting process was also performed. The results demonstrate that the power demand during cutting is consistent with theoretical calculations, and that the designed cutting device meets both the power requirements and the operational specifications for shrub pruning.

This study introduced the Focal‑CIoU loss function into the YOLOv5s model and developed a shrub target detection model specifically tailored for desert environments with sparse backgrounds. The improved model achieves an accuracy of 91.9%, a recall of 96.5%, and an mAP@0.5 of 98.3%. While significantly enhancing detection performance, the model maintains a low parameter count, which is sufficient to meet the real‑time detection requirements of the shrub pruning machine.

Based on image processing and binocular stereo vision, this study achieved shrub root region segmentation and three-dimensional coordinate estimation. Experimental results demonstrate that under complex background conditions, the proposed shrub root detection method robustly extracts root contours. The maximum relative errors for depth and height measurements are 3.19% and 6.51%, respectively—both within the positioning accuracy tolerance required for shrub pruning operations.

ACKNOWLEDGEMENT

This work was supported by the Major Science and Technology Project of Inner Mongolia Autonomous Region (2020ZD0002).

REFERENCES

[1] Almatrouk B., Meng H., & Swash M.R. (2024). Holoscopic elemental-image-based disparity estimation using multi-scale, multi-window semi-global block matching, *Applied Sciences*, vol.14, no.8, Article 3335, London/United Kingdom. https://doi.org/10.3390/app14083335

[2] Cao N., & Liu Y. (2024). High-noise grayscale image denoising using an improved median filter for the adaptive selection of a threshold, *Applied Sciences*, vol.14, no.2, Article 635, Zhengzhou/China. https://doi.org/10.3390/app14020635

[3] Chun P., Izumi S., & Yamane T. (2021). Automatic detection method of cracks from concrete surface imagery using two-step light gradient boosting machine, *Computer-Aided Civil and Infrastructure Engineering*, vol.36, no.1, pp.61-72, Tokyo/Japan. https://doi.org/10.1111/mice.12564

[4] Fan X.P., Xu Y., & Zhou J.P. (2025). Visual navigation method and field experiment of a cotton field spraying robot (棉田施药机器人视觉导航方法与田间试验), *Transactions of the Chinese Society of Agricultural Engineering*, vol.41, no.6, pp.52-61, Beijing/China. https://doi.org/10.11975/j.issn.1002-6819.202408183

[5] Gangwar T., & Schillinger D. (2019). Microimaging-informed continuum micromechanics accurately predicts macroscopic stiffness and strength properties of hierarchical plant culm materials, *Mechanics of Materials*, vol.130, pp.39-57, Twin Cities/USA. https://doi.org/10.1016/j.mechmat.2019.01.009

[6] Gao S., Wu J., Ma L., Gong X., & Zhang Q. (2023). Introduction to sand-restoration technology and model in China, *Sustainability*, vol.15, no.1, Article 98, Hohhot/China. https://doi.org/10.3390/su15010098

[7] Georges R., Auchet S., & Méausoone P.J. (2014). A dynamic measurement of a disc chipper cutting forces, *Biomass and Bioenergy*, vol.64, pp.269-275, Reggio Calabria/Italy. https://doi.org/10.1016/j.biombioe.2014.02.033

[8] Hu J., Wang H., Zhou Y., Yang S., Lv H., & Yang L. (2024). Research on internal quality testing method of dry longan based on terahertz imaging detection technology, *Journal of Food Measurement and Characterization*, vol.18, no.7, pp.5507-5522, Nanchang/China. https://doi.org/10.1007/s11694-024-02583-x

[9] Hu W., Wang W., Ai C., Wang J., Wang W., Meng X., Liu H., Tao H., & Qiu S. (2021). Machine vision-based surface crack analysis for transportation infrastructure, Automation in Construction, vol.132, Article 103973, Changsha/China. https://doi.org/10.1016/j.autcon.2021.103973

[10] Johnson P.C., Clementson C.L., Mathanker S.K., Grift T.E., & Hansen A.C. (2012). Cutting energy characteristics of *Miscanthus* × *giganteus* stems with varying oblique angle and cutting speed, *Biosystems Engineering*, vol.112, no.1, pp.42-48, Urbana IL/USA. https://doi.org/10.1016/j.biosystemseng.2012.02.003

[11] Li T., Ren L., Hu B., Wang S., Zhao M., Zhang Y., & Yang M. (2023). Grading detection of tomato hole-pan seedlings using improved YOLOv5s and transfer learning (改进 YOLOv5s 和迁移学习对番茄穴盘苗的分级检测), *Transactions of the Chinese Society of Agricultural Engineering*, vol.39, no.23, pp.174-184, Xinjiang/China. https://doi.org/10.11975/j.issn.1002-6819.202308078

[12] Ma A.J., Chen Z.J., Yu G.S., Yuan X.Y., & Du K. (2015). Development and application of a crawler self-propelled stubble cutter for desert shrub forest (履带自行式沙地灌木林平茬机的研制及应用), *Scientia Silvae Sinicae*, vol.51, no.7, pp.99-106, Beijing/China. https://doi.org/10.11707/j.1001-7488.20150711

[13] Mutlu H. (2021). Design of the crank-rocker mechanism for various design cases based on the closed-form solution, *Sādhanā*, vol.46, Article 4, Mersin/Turkey. https://doi.org/10.1007/s12046-020-01529-5

[14] Pei Z.Y., Duan G.D., Hao S.R., Qiao J.W., & Qin W. (2019). Optimization of stumping method based on wind control benefit for *Salix psammophila* shrub in Mu Us sandy land (基于防风效益的毛乌素沙地沙柳灌丛平茬方法优选), *Transactions of the Chinese Society of Agricultural Engineering*, vol.35, no.4, pp.153-161, Hohhot/China. https://doi.org/10.11975/j.issn.1002-6819.2019.04.019

[15] Peng H., Liang M., Yuan C., & Ma Y. (2024). EDF-YOLOv5: An improved algorithm for power transmission line defect detection based on YOLOv5, *Electronics*, vol.13, no.1, Article 148, Zhengzhou/China. https://doi.org/10.3390/electronics13010148

[16] Ren K. (2021). *Machine vision technology for Caragana stubble cutting machine (柠条平茬机的机器视觉技术研究)*, MSc thesis, Harbin Engineering University, Harbin/China.

[17] Ren Z., Fang F., Yan N., & Wu Y. (2022). State of the art in defect detection based on machine vision, *International Journal of Precision Engineering and Manufacturing-Green Technology*, vol.9, no.2, pp.661-691, Tianjin/China. https://doi.org/10.1007/s40684-021-00343-6

[18] Tian Z.Q. (2013). Development status and trend of Caragana shrub harvester (柠条收割机发展现状及趋势), *Agricultural Engineering*, no.4, pp.9-11, Jinzhong/China.

[19] Wang Q., Yan C., Tan R., Feng Y., Sun Y., & Liu Y. (2022). 3D-CALI: Automatic calibration for camera and LiDAR using 3D checkerboard, *Measurement*, vol.203, Article 111971, Nanjing/China. https://doi.org/10.1016/j.measurement.2022.111971

[20] Wang Y., Zhang J., Gao Y., Qu A., Wen X., & Hou Y. (2025). Design and test of the hydraulic shear-type *Caragana korshinskii* Kom. coppicing machine (液压剪式柠条平茬机的设计与试验), *Transactions of the Chinese Society of Agricultural Engineering*, vol.41, no.14, pp.71-81, Yinchuan/China. https://doi.org/10.11975/j.issn.1002-6819.202412022

[21] Wu G., & Zhang D.D. (2022). Thermal-mechanical coupling analysis of disc brake based on ANSYS Workbench (基于 ANSYS Workbench 的盘式制动器热机耦合分析), *Lubrication Engineering*, vol.47, no.10, pp.126-133, Yichang/China. https://doi.org/10.3969/j.issn.0254-0150.2022.10.018

[22] Zhai G., Zhang W., Hu W., & Ji Z. (2020). Coal mine rescue robots based on binocular vision: A review of the state of the art, *IEEE Access*, vol.8, pp.130561-130575, Beijing/China. https://doi.org/10.1109/ACCESS.2020.3009387

[23] Zhang B., Liu Y., Zhang H., Shen C., & Fu W. (2022). Design and evaluation of a shaping and pruning machine for dwarf and densely planted jujube trees, *Applied Sciences*, vol.12, no.5, Article 2699, Haikou/China. https://doi.org/10.3390/app12052699

[24] Zhou R.G., Chang Z.B., Fan P., Li W., & Huan T.T. (2015). Quantum image morphology processing based on quantum set operation, *International Journal of Theoretical Physics*, vol.54, no.6, pp.1974-1986, Nanchang/China. https://doi.org/10.1007/s10773-014-2402-4